

# NiAl Oxidation Reaction Processes Studied In Situ Using MEMS-Based Closed-Cell Gas Reaction Transmission Electron Microscopy

Kinga A. Unocic<sup>1</sup>  · Dongwon Shin<sup>1</sup> · Raymond R. Unocic<sup>2</sup> · Lawrence F. Allard<sup>1</sup>

Received: 15 November 2016 / Published online: 7 February 2017  
© Springer Science+Business Media New York (outside the USA) 2017

**Abstract** The nanoscale oxidation mechanisms and kinetics of a model  $\beta$ -NiAl system were investigated using in situ closed-cell gas reaction scanning transmission electron microscopy (STEM). Here, we directly visualize the dynamic structural and chemical changes that occur during high-temperature oxidation at a high spatial resolution of 50.3Ni–49.7Al (at.%) nanoparticles under static air conditions at 730 Torr with heating up to 750 °C at 5 °C/s. A MEMS-based gas cell system, with microfabricated heater devices and a gas delivery system, was used to reveal site-specific oxidation initiation sites. Through time-resolved annular dark-field STEM imaging, we tracked the nanoscale oxidation kinetics of  $\text{Al}_2\text{O}_3$ . After oxidation at 750 °C, nucleation of voids at the Ni/ $\text{Al}_2\text{O}_3$  interface was observed along a NiAl grain boundary, followed by the formation of faceted NiO crystals. Small faceted cubic crystals of NiO were formed at the initial stage of oxidation at high  $\text{PO}_2$  due to the outward self-diffusion of  $\text{Ni}^{2+}$  ions, followed by the formation of a

---

**Electronic supplementary material** The online version of this article (doi:[10.1007/s11085-016-9676-2](https://doi.org/10.1007/s11085-016-9676-2)) contains supplementary material, which is available to authorized users.

---

✉ Kinga A. Unocic  
unocicka@ornl.gov

Dongwon Shin  
shind@ornl.gov

Raymond R. Unocic  
unocicrr@ornl.gov

Lawrence F. Allard  
allardlfjr@ornl.gov

<sup>1</sup> Materials Science & Technology Division, Oak Ridge National Laboratory, 1 Bethel Valley Road, Oak Ridge, TN 37831, USA

<sup>2</sup> Center For Nanophase Materials Sciences Division, 1 Bethel Valley Road, Oak Ridge, TN 37831, USA

mixture of metastable and stable  $\alpha$ -Al<sub>2</sub>O<sub>3</sub> at the oxide/metal interface that is attributed to a PO<sub>2</sub> decrease with oxidation time, which agreed with thermodynamic modeling calculations. The results from these in situ oxidation experiments in the  $\beta$ -NiAl system are in agreement with the established oxidation mechanisms; however, with in situ closed-cell gas microscopy it is now feasible to investigate nanoscale oxidation mechanisms and kinetics in real time and at high spatial resolution and can be broadly applied to understand the basic high-temperature oxidation mechanisms for a wide range of alloy compositions.

**Keywords** NiAl · Oxidation · In situ TEM · MEMS-based closed-cell gas

## Introduction

Nickel aluminides ( $\beta$ -NiAl) are high-temperature structural materials that have found application as thermal barrier coatings in hot-section gas turbine engine components due to their high melting temperature and oxidation resistance in aggressive environments [1]. The excellent oxidation resistance behavior is attributed to the formation of a stable, slow-growing  $\alpha$ -Al<sub>2</sub>O<sub>3</sub> scale [2]. Mechanistically, in the early stages of oxidation and/or at lower temperatures ( $\leq 1100$  °C) [3], metastable  $\gamma$ ,  $\delta$ , or  $\theta$ -Al<sub>2</sub>O<sub>3</sub> oxides initially form upon exposure to the atmosphere by the outward transport of Al<sup>3+</sup> and Ni<sup>2+</sup> ions to the gas/NiAl surface, and their instant interaction with oxygen. The metastable Al<sub>2</sub>O<sub>3</sub> nuclei grow until a complete healing layer of  $\alpha$ -Al<sub>2</sub>O<sub>3</sub> forms underneath, which grows mainly by oxygen transport along alumina grain boundaries and nucleates at the scale/alloy interface. Because Al<sub>2</sub>O<sub>3</sub> is a polymorph, eventually the metastable Al<sub>2</sub>O<sub>3</sub> phases transform into a thermodynamically stable  $\alpha$ -Al<sub>2</sub>O<sub>3</sub>. The transformation from the metastable phases into the stable  $\alpha$ -Al<sub>2</sub>O<sub>3</sub> is dependent on the interplay between factors such as temperature, oxygen partial pressure, grain boundary density, and grain boundary chemistry. The oxidation resistance of  $\beta$ -NiAl can be further improved by alloying with refractory metals (e.g., chromium, molybdenum) [4] and by the addition of reactive elements (REs) such as Y, Hf, and Zr that alter the  $\theta$ -Al<sub>2</sub>O<sub>3</sub> to  $\alpha$ -Al<sub>2</sub>O<sub>3</sub> transformation kinetics [5] and/or effectively decrease or block the oxide grain boundary diffusion pathways [6–8].

Although the rate-controlling mechanisms and kinetics of Al<sub>2</sub>O<sub>3</sub> scale formation have been well studied using thermogravimetric methods and post-exposure microstructural evaluation, there is at present a lack of experiments conducted in situ that have the capability to directly image the nanoscale oxidation behavior during thermal exposure and under oxidizing conditions. Modern in situ electron microscopy techniques have evolved such that it is now feasible to directly image oxidation processes at high spatial resolution, by analyzing the dynamic structural changes at metal–oxide interfaces. There are two ways to perform in situ microscopy experiments. The in situ environmental TEM (ETEM) is a method that utilizes differential pumping apertures to permit the controlled leaking of reactant gases at pressures up to a few Torr into the high-vacuum environment of the TEM column [9, 10]. When coupled with an in situ TEM *heating* holder, oxidation

processes can be visualized and the rate-controlling oxidation mechanisms can be determined [9–11]. An alternative to in situ ETEM approach is to utilize a “closed-form” environmental gas-cell holder for in situ scanning/transmission electron microscopy (S/TEM) oxidation studies. The primary advantage is that the holder allows reactions to be conducted at gas pressures in the range of  $7.6 \times 10^{-4}$  to 760 Torr as opposed to only a few Torr when compared to ETEM. Furthermore, these systems utilize thin-film, MEMS-based heaters that allow for controlled heating and cooling at rates up to 1000 °C per millisecond. The low mass and low power of the MEMS heaters provide rapid temperature stabilization and concomitant drift stabilization so that the ultimate resolution capability of the electron microscope is not compromised [12–14].

The aim of this study is to demonstrate the powerful analytical capabilities of an in situ environmental cell for high-resolution scanning transmission electron microscopy studies of the initial stages of high-temperature oxidation. We used the in situ closed-cell gas reactor system to investigate the structural and chemical evolution of well-characterized  $\beta$ -NiAl during thermal exposure and under oxidizing conditions. The oxidation processes are directly imaged from the in situ S/TEM imaging using high-angle annual dark-field (HAADF) and bright-field (BF) STEM image modes, while the chemical composition (following exposure) is determined through energy dispersive X-ray spectroscopy (EDS).

## Experimental Procedures

A commercial Protochips Atmosphere 200™ environmental gas cell system was used to investigate the oxidation mechanisms in  $\beta$ -NiAl. The environmental gas cell portion of the system is composed of a pair of microfabricated silicon microchip devices (“heating chip” (Fig. 1a, b) and “window”) with gold contacts and electron-transparent SiN membranes ( $\sim 30$  nm thick and  $\sim 50$  nm thick, respectively) that are stacked together to seal a thin layer of gas (Fig. 1c). Further details are reported elsewhere [12]. One device (“E-chip”) features an integrated low-conductivity SiC ceramic membrane (300–500  $\mu\text{m}$  square) placed over a hole etched

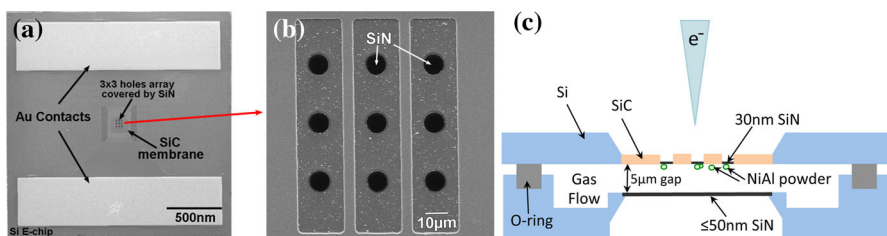


**Fig. 1** Secondary electron image of **a** the E-chip heating device showing **b** a higher magnification of the center of a  $3 \times 3$  array of  $8\text{-}\mu\text{m}$ -diameter holes patterned in the thin, low-conductivity SiC ceramic membrane, covered by amorphous SiN. **c** Schematic of the cross-section of the closed-cell gas-reaction holder with an E-chip on the *top* and a window device on the *bottom* with an O-ring in-between to provide a gas-sealed environment

into a Si chip and Au contacts deposited on the Si chip to allow for resistive heating of the SiC membrane (Fig. 1a, b). The thin-film heater allows specimens to be heated to temperatures up to 1000 °C in milliseconds through resistance heating by passing current [12]. Each E-chip is calibrated using infrared imaging methods (Mikron M9103 IR camera), with a measurement accuracy of  $\pm 5\%$  claimed by Protochips Co. Every E-chip also includes a  $3 \times 3$  array of 8- $\mu\text{m}$ -diameter holes patterned in the thin, low-conductivity SiC ceramic membrane, which are covered by amorphous SiN (Fig. 1b). This SiN serves as the specimen support and regions of electron transparency for observations of structural and chemical changes during the reaction. A gas handling manifold with an electronic control system is operated via a custom workflow-based software package and is used to deliver gases to the holder during elevated temperature reaction experiments. The gas handling system is composed of three gas input lines, two experimental gas holding tanks, and a receiving tank for gas flow control during the experiment. The E-chips are temperature-calibrated via a method that is independent of gas composition and pressure, thereby providing control of reaction temperatures under any chosen gas conditions.

NiAl powder, with a chemical composition of 50.3Ni–49.7Al at.% (American Elements) and a starting mesh size of 325, was crushed in methanol using a mortar and pestle to decrease the particle size scale to 5 microns or less. The powder was then deposited onto the thin-film heater device portion of the E-chip device (Fig. 1a, b) to yield some NiAl particles distributed over the electron-transparent SiN membrane. The E-chip becomes the top (i.e., incident beam side Fig. 1c) element of the gas cell stack, with an electron-transparent amorphous SiN window device as the bottom element (Fig. 1c). The devices are clamped in the holder tip, against a double o-ring arrangement to provide a gas-sealed environment. An aberration-corrected JEOL 2200FS STEM, equipped with a CEOS GmbH corrector on the probe-forming lenses and operating at 200 kV, was used for simultaneous BF and HAADF–STEM imaging. For imaging, the convergence semi-angle was 26.5 mrad with an inner and an outer collection semi-angle of 110 and 470 mrad, respectively, for the HAADF–STEM detector. The beam current was nominally 150 pA. Because the sample particles are retained on the lower side of a nominal 30-nm-thick SiN window, the electron beam only “sees” the window material before impinging on the sample, with subsequent imaging realized just by collecting the forward and high-angle scattered electrons; thus, resolution even at a full atmosphere is scarcely compromised (e.g., atomic column resolution has been shown at high temperature and pressure in many systems [12]). The in situ “lab air” oxidation experiment was performed in laboratory air under static gas conditions of 730 Torr with incremental/step heating up to 750 °C. The heating rate between the steps was  $\sim 5$  °C/s. Following the heating experiments, the chemical composition of the oxidation products was analyzed using the JEOL 2200FS operating at 200 kV and equipped with Bruker EDS system. A computational thermodynamic approach was used to investigate the effect of oxygen partial pressure on the phase stability of  $\beta$ -NiAl. Thermodynamic descriptions for the Ni–Al–O ternary system were taken from the TCNI8 database as implemented in Thermo-Calc software package.

## Results and Discussion

### Incremental/Step Heating Up to 750 °C in Air at 730 Torr

The structure and chemistry of a  $\beta$ -NiAl nanoparticle was analyzed before, during, and after in situ TEM oxidation experiments using STEM–EDS [14]. The temperature profile during the experiments that was recorded by the system controller is presented in Fig. 2a. This data can be directly linked to the STEM images acquired during thermal exposure. Figure 2b shows HAADF–STEM images of the NiAl starting microstructure imaged at 300 °C in vacuum, which is irregularly shaped and varies in thickness. Imaging at 300 °C helped to prevent contamination. STEM–EDS mapping, before placing the specimen into the closed-cell gas reactor, indicated a homogenous distribution of Ni and Al throughout the entire particle. As expected, the surface of the particle was slightly oxidized as evidenced by the presence of native oxide (oxygen EDS map in Fig. 2b). The particle contained a very thin ( $\sim 4$  nm) native film of either NiO,  $\text{Al}_2\text{O}_3$  or mixture of both. This is expected because an oxide can form when the NiAl surface is exposed at room temperature in air during handling [11]. This particle was heated in the gas cell under 730 Torr first to 600 °C with 5 °C/s and monitored, then to 700 °C (monitored), and finally at 750 °C. Figure 2c shows the same NiAl particle after in situ step oxidation to 750 °C in air at 730 Torr with corresponding EDS maps. There is a noticeable change in the NiAl particle morphology. At locations where an Al-rich oxide (further discussed later) formed, there are localized regions of randomly distributed Ni enrichment. Comparison of Ni EDS maps before and after oxidation demonstrates that the size of the NiAl particle decreased, suggesting that the inward diffusion of  $\text{Ni}^{2+}$  ions and the outward diffusion (to the oxide/metal interface) of  $\text{Al}^{3+}$  occurred.

To elucidate the oxidation kinetics, a time-lapsed series of HAADF–STEM images was acquired during thermal exposure at 700 °C (Fig. 3a) and 750 °C (Fig. 3b). The elapsed time at temperature is overlaid on each image, which is correlated with the temperature profile in Fig. 2a. As expected, the reaction kinetics increased with the increasing temperature. Comparing the oxidation kinetics

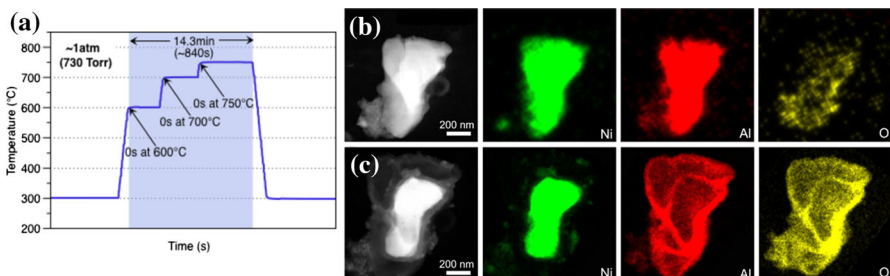


**Fig. 2** **a** Temperature profile from the in situ closed-cell gas reaction step oxidation showing the accuracy of measured temperature and step heating. **b** HAADF–STEM with EDS mapping of  $\beta$ -NiAl particle. **c** HAADF–STEM with EDS mapping of  $\beta$ -NiAl particle after step oxidation to 750 °C in air at 730 Torr

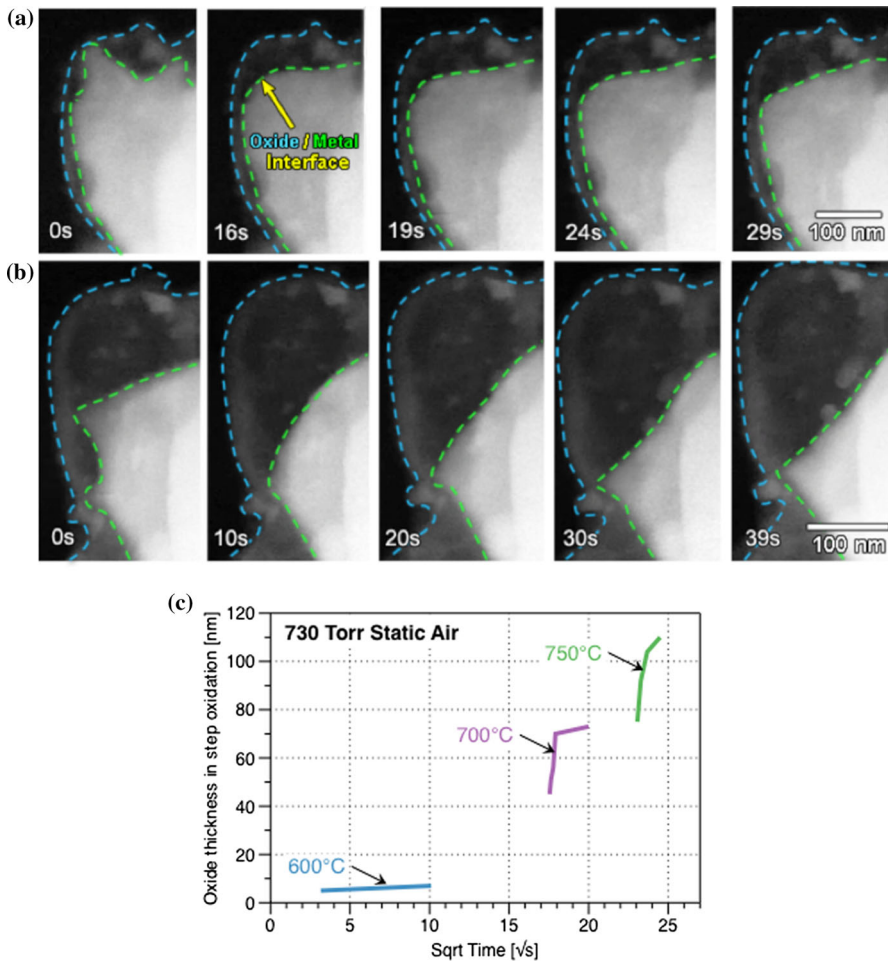


**Fig. 3** A time-lapsed series of HAADF-STEM images showing the oxidation behavior of  $\beta$ -NiAl at **a** 700 °C and **b** 750 °C in static air at 730 Torr. **c** Measured oxide scale thickness at three different temperatures (650, 700, and 750 °C) as a function of time formed on NiAl during oxidation in air at 730 Torr

between 600, 700, and 750 °C, there is minimal oxidation that was observed at 600 °C (being the slowest; not shown here). At 750 °C, the dynamics of the oxidation reactions were the most vigorous due to faster diffusion of elements than at lower temperatures (600 and 700 °C). This can be seen when examining the corresponding HAADF-STEM images. Brightness in HAADF-STEM imaging increases with both atomic number and thickness [15]. Therefore, the brightest area indicates an oxidized NiAl particle, and as time elapses the interface between oxide and NiAl migrates inward into NiAl particle core. As a consequence, the oxidation product formed on the NiAl particle was much thinner at 600 and 700 °C than it was at 750 °C. Also, this study shows that at all three temperatures the oxidation product

was not uniform in thickness around the particle (location specific). This was often due to the different thicknesses of the NiAl particle resulting in faster metal exhaustion in the thinnest areas. A benefit of the in situ closed-cell gas reaction experiments is to be able to determine site-specific nucleation and growth locations of the oxide. Oxidation often originated at the corners of the NiAl particles, in the thinner areas, where the depletion in Al most likely occurred and further supply of Al was not available (loss of the Al reservoir). Figures 3a, b shows the non-uniform nature of oxidation of the NiAl particle after the final stage of oxidation. The NiAl particle is a 3-dimensional (3D) structure; however, the STEM images are a 2D projection with the oxide formed out of plane not clearly distinguishable. As expected, much faster “consumption”/oxidation of the NiAl particle was noticed at 750 °C (Fig. 3c) due to faster diffusion of the elements and inward oxide growth due to oxygen diffusion through the scale and interaction at the oxide/metal interface.

A summary of the measurements of the scale thickness generated from one location (change in the same area per temperature) is shown in Fig. 3c. The measurements were performed at 600, 700, and 750 °C; thus, the measurements at higher temperatures also contain the oxide scale thickness formed on the NiAl particle at lower temperatures. This is not the ideal measurement method; however, it demonstrates that the oxide growth can be monitored step by step. As expected, the thinner oxide was formed at lower temperature. The initial rate of oxidation was faster at higher temperatures (750 °C) with a decrease in oxidation rate (plateau) being reached within a shorter time (Fig. 3c). At higher temperature (750 °C), fast initial oxidation is due to the increased diffusion rate of the  $\text{Ni}^{2+}$  and  $\text{Al}^{3+}$  ions to the surface and the subsequent quicker establishment of the protective oxide ( $\text{Al}_2\text{O}_3$  layer) with the decreasing oxygen partial pressure from the oxide/metal interface. At lower temperature, the diffusion of  $\text{Ni}^{2+}$  and  $\text{Al}^{3+}$  ions is slower, and, therefore, establishing the protective oxide scale requires longer time [3]. The identification of the oxide scale at lower temperature was not possible because the exposure at 700 °C was immediately followed by exposure at 750 °C. It is presumed that the oxide formed at 700 °C was most likely metastable  $\text{Al}_2\text{O}_3$ , since it has been reported that metastable  $\text{Al}_2\text{O}_3$  forms at lower temperatures but at higher rates when compared to  $\alpha$ - $\text{Al}_2\text{O}_3$  [3, 4].

### Structural, Analytical, and Quantitative Analyses

Following thermal exposure, the structure and chemical composition of the oxide film were analyzed using computed diffractograms from high-resolution lattice images, and EDS chemical analysis. The entire surface of the NiAl particle was oxidized in 3D (including the direction out of plane (surface of the NiAl)) and the oxide structure was composed of nanograins as shown in the BF-STEM image in Fig. 4a. In Fig. 4b, the diffractogram from the image showed periodicities with a measured d-spacing of 0.2403 nm, which corresponds to the {311} d-spacing of metastable  $\gamma$ - $\text{Al}_2\text{O}_3$  (according to International Center for Diffraction Data (ICDD) diffraction PDF<sup>#</sup> 00-047-1292) with a reported d-spacing of 0.2396 nm. The diffractogram generated from a different oxide area showed periodicities that

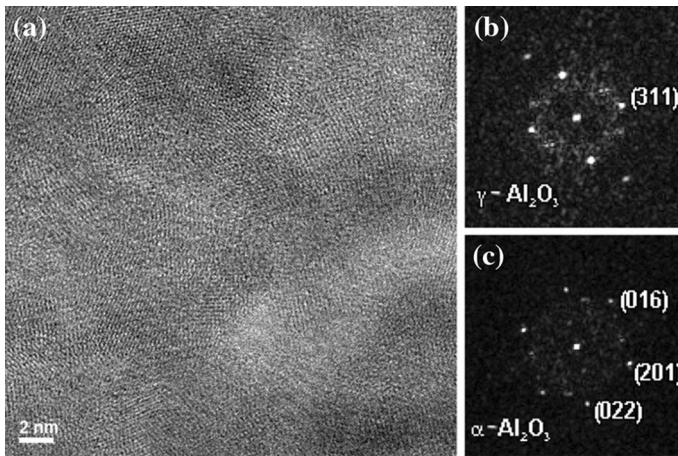


**Fig. 4** **a** High-resolution BF-STEM image showing the nanograin structure of the oxide formed after in situ step heating in air at 730 Torr up to 750 °C. FFTs generated from different locations of the oxide are a mixture of **b** cubic ( $Fm\bar{3}m$ )  $\gamma$ - $Al_2O_3$  and **c** hexagonal ( $R\bar{3}c$ )  $\alpha$ - $Al_2O_3$  corundum (reported in the three-index hkl notation)

measured 0.2025, 0.1938, and 0.1972 nm, which correspond well with  $\alpha$ - $Al_2O_3$  d-spacings. The interplanar spacings for  $\alpha$ - $Al_2O_3$  (from ICDD PDF# 00-041-1475; 00-033-1161) and the measured values are summarized in Table 1. Combining this structural information with EDS analysis further confirms the existence of  $Al_2O_3$  but this structural analysis shows that the oxide is in fact a mixture of metastable  $\gamma$ - $Al_2O_3$  and stable  $\alpha$ - $Al_2O_3$ .

Interestingly, faceted and randomly distributed nanocrystals ( $\sim 25$  nm) were present along the gas/oxide interface. An example of a small  $\sim 25$ -nm faceted crystal formed on the surface of nanograin  $Al_2O_3$  along with the corresponding EDS elemental maps after in situ oxidation experiments of NiAl (bottom part) is shown in Fig. 5. EDS chemical maps and EDS line profiles showed that the faceted crystals are mainly enriched in O and Ni. Further, the diffractogram generated from the faceted crystal (bottom inset in Fig. 5b) showed lattice planes with the measured d-spacing of 0.1479 nm which is in acceptable agreement with the published diffraction values by ICDD (PDF# 00-004-0835) for NiO (0.1476 nm), corresponding to  $\{220\}$  spacings. Combining this information with EDS results further supports the finding that the faceted oxide is a cubic NiO with an  $Fm\bar{3}m$  space group

**Table 1** Measured and ICDD (PDF# 00-041-1475; 00-033-1161) interplanar distances (d) obtained from the oxide scale formed after in situ oxidation of NiAl particle using step heating to 750 °C in air at 730 Torr using three-index hkl notation

d [Å]	$d_1(201)$	$d_2(022)$	$d_3(016)$	$\alpha_{12}$ (°)	$\alpha_{13}$ (°)
Measured	0.2025	0.1938	0.1972	60.1	69.7
$\alpha$ - $Al_2O_3$	0.2035	0.1964	0.1917	60.4	68.3



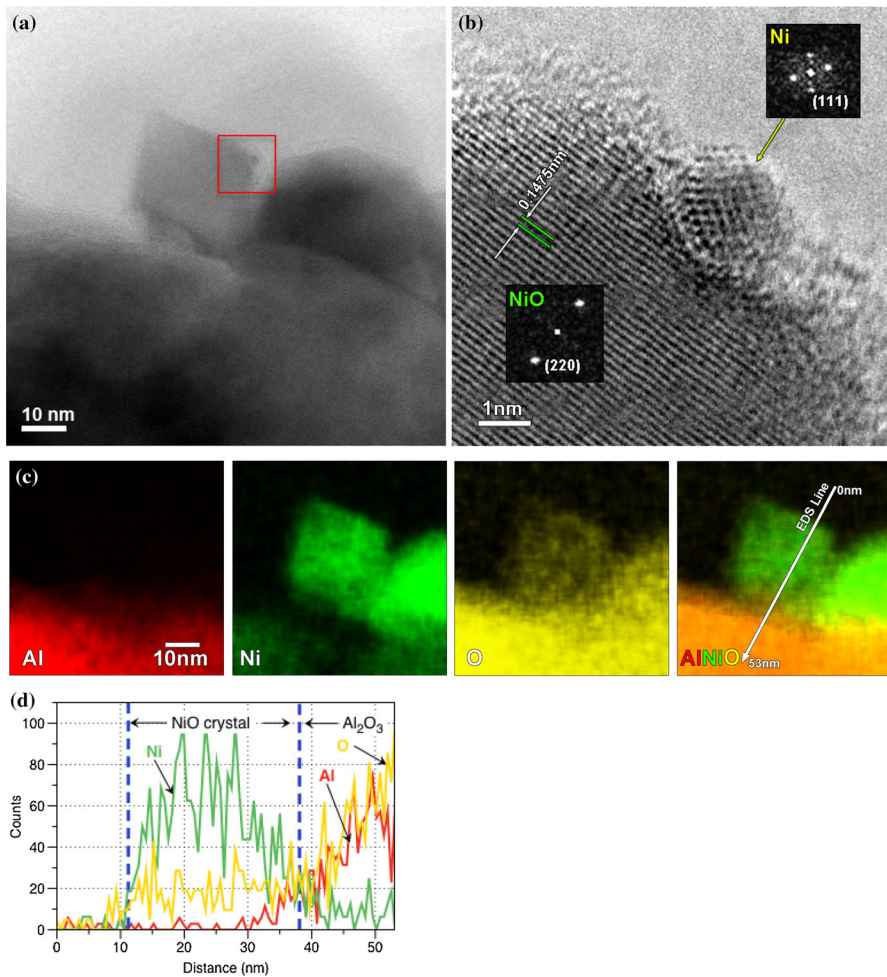


**Fig. 5** **a** BF-STEM and **b** high-resolution BF-STEM image with the corresponding **c** EDS maps of the faceted crystals formed at the gas/oxide interface and **d** EDS line profiles for Ni, Al, and O across the faceted crystal that formed on the surface of oxide scale in air after step heating to 750 °C

and 0.4177 nm lattice parameter. During the initial stages of oxidation, the oxygen partial pressure ( $P_{O_2}$ ) is expected to be high at the gas/metal interface, which allows for oxidation of Ni and Al when they come into contact with the atmosphere. Thermodynamic modeling, described in more detail later, predicted that at higher oxygen partial pressures (between 1 and  $10^{-16}$  atm) fcc Ni can be oxidized to halite (NiO), while  $\beta$ -NiAl would oxidize to the spinel  $NiAl_2O_4$  and/or  $Al_2O_3$ . The presence of faceted NiO crystals indicated that they formed at the initial stage of oxidation somewhere between 1 and  $10^{-16}$  atm from the fcc Ni substrate. Wood and Chattopadhyay [16] showed the formation of NiO within very short exposure times (2.5–10 min) at 600 °C in NiAl alloys. The authors investigated the oxidation behavior of NiAl alloys with various Al contents (from Ni-2.2 at.% Al to

Ni-22.9 at.% Al) at 600 °C and found that NiO formed in all alloys and the relative amount diminished as the alloy's Al content was increased. Thus, in our study NiO was probably formed either due to fast local selective oxidation of Ni in initial oxidation due to high PO<sub>2</sub> or because of the local depletion in Al from the NiAl substrate. These results show the benefit of this technique, which is to have the ability to characterize local variations in the oxide scale that often might be missed due to low spatial resolution characterization techniques, or long exposures times that result either in oxide transformation or its partial spallation. No spinel oxide (NiAl<sub>2</sub>O<sub>4</sub>) was found [16, 17] but we cannot exclude the fact that it did not form since the analytical and structural analyses were carried out after final oxidation at 750 °C. Along the surface of the faceted NiO nanocrystals, a small (less than 3-nm) particle was found (Fig. 5a). The diffractogram from this particle is shown in the inset of Fig. 5b, which indicates that the particle is oriented along the [1 $\bar{1}$ 0] zone axis. The measured d-spacing of 0.2073 nm corresponds to {111}-type spacings that matched with the cubic Ni, Fm $\bar{3}$ m space group with 0.2035 nm lattice parameter. The values of measured and ICDD (PDF# 04-001-1136) interplanar spacings (d) and angles (open square) for small spherical particle found on the faceted NiO are summarized in Table 2. Most likely, this was an isolated material from the substrate that was trapped during initial oxidation since the reaction was very fast at the initial stage of oxidation.

### Void formation and Scale Damage

After oxidation for 92 s in static air at 750 °C, void formation was observed at the NiAl/Al<sub>2</sub>O<sub>3</sub> interface. The location of void formation is marked with purple arrows in Fig. 6. Here, we interpret these observations as the outward diffusion of Ni<sup>2+</sup> ions (as indicated by the yellow arrows in images from 129 s through 158 s) since Al was most likely exhausted at this stage to support reformation of the Al<sub>2</sub>O<sub>3</sub> scale. Diffusion of Ni<sup>2+</sup> ions (refer to supplementary video) that appeared along a NiAl grain boundary resulted in the formation of faceted nanocrystals at the interface. Outward diffusion of Ni<sup>2+</sup> ions was monitored step by step due to the ability to record these changes in situ, which allowed us to identify site-specific interfacial locations where this occurred, as well as the kinetics of crystal growth, and also to monitor the morphology of the crystals over time at high temperature. A higher magnification image of the faceted nanocrystals is shown in Fig. 7a. The corresponding EDS maps and EDS line profile shown in Fig. 7b and Fig. 7c,

**Table 2** Measured and ICDD (PDF# 04-001-1136) interplanar spacings (d) and angles ( $\alpha$ ) for the small spherical particle found on the faceted NiO in Fig. 5b which was analyzed after in situ oxidation of NiAl particle using step heating to 750 °C in air at 730 Torr

D [Å]	d <sub>1</sub> (111)	d <sub>2</sub> ( $\bar{1}\bar{1}\bar{1}$ )	$\alpha_{13}$ (°)	$\alpha_{23}$ (°)
Measured	2.073	1.983	70.4	109.6
Ni	2.035	2.035	70.5	109.5

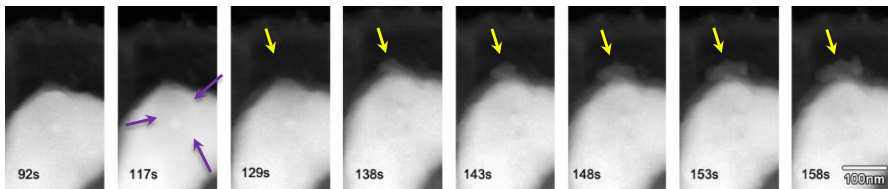


**Fig. 6** A time-lapsed series of HAADF-STEM images showing site-specific location for oxidation at 750 °C in static air at 730 Torr. *Purple arrows* point to the void present in the structure, while *yellow arrows* point to the formation of the faceted NiO crystals (Color figure online)

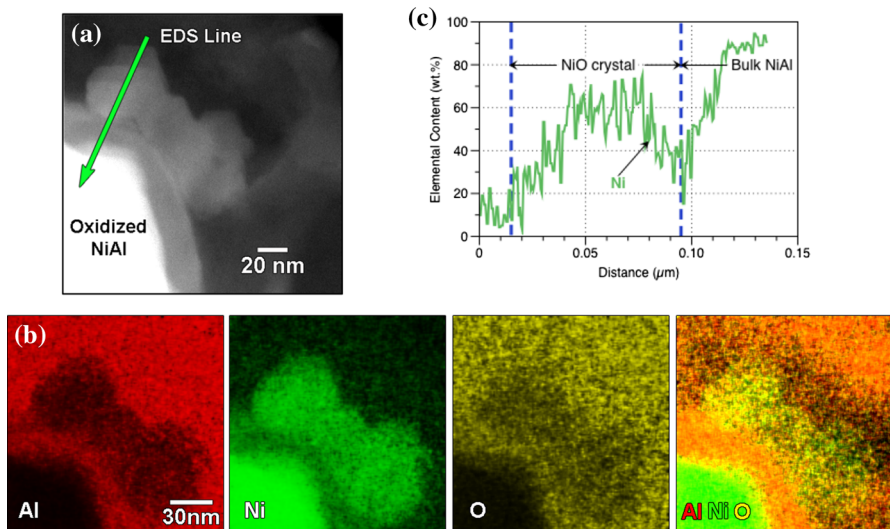


**Fig. 7** **a** HAADF-STEM image with the corresponding **b** EDS maps and **c** EDS line profile generated from the location marked in the HAADF-STEM image in (a)

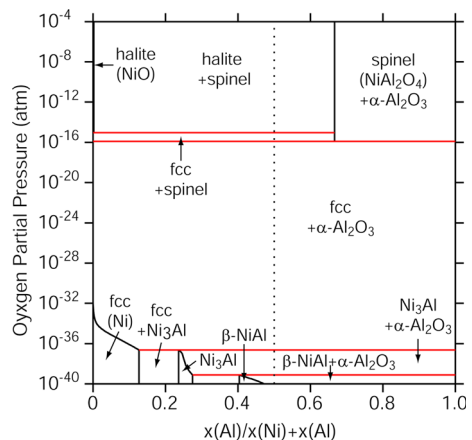
respectively, revealed the enrichment of Ni and O. The high-resolution image was not obtained due to beam contamination of the area. However, it can be observed from the EDS maps that similar NiO crystals, as identified in Fig. 7, formed at the oxide/metal interface when the detachment of the oxide scale occurred. Void formation has widely been studied [18–20] and is often reported as being attributed to high diffusivity of  $\text{Al}^{3+}$  ions compared with the lower inward diffusion rate of  $\text{O}^{2-}$  ions through the scale to the oxide/metal interface and the inward/back diffusion of  $\text{Ni}^{2+}$  ions resulting in void formation due to the Kirkendall effect [18]. Further, it is well established that there is a “critical” concentration of protective elements (e.g., Al) to form a slow-growing oxide layer [21]. In general, at high temperature and depending on the material system, the oxidation resistance of the alloys depends on the ability to form protective surface scales (e.g.,  $\text{Al}_2\text{O}_3$  or  $\text{Cr}_2\text{O}_3$ ) during service. The depletion in the scale-forming elements (e.g., Al or Cr) in the bulk alloy is mainly due to scale growth and scale re-healing after spallation (in our case void formation). If the concentration of Al decreases below a critical level,

oxidation of the base/bulk elements (e.g., Ni), which form less protective oxide scales, follows, leading to catastrophic oxidation of the metallic component. The formation of NiO crystals in the later stage of oxidation suggests that Al concentration (reservoir in NiAl particle) reached the critical value, and further formation of alumina is not possible. Increasing the thickness of the particle (e.g., at large laboratory scale, thickness of the component) should extend the lifetime due to greater reservoir supply. However, it should be noted that the goal was not to intentionally form a protective oxide layer but, rather, to study the degradation and dynamic reactions using in situ electron microscopy.

## Thermodynamic Calculations

We have used the computational thermodynamic approach to further investigate the effect of oxygen partial pressure on the phase stability of  $\beta$ -NiAl. The structural and chemical evolution from in situ oxidation experiments has been elucidated using the TCNI8 database as implemented in the Thermo-Calc software package. Figure 8 shows the calculated phase diagram at 750 °C and different partial pressures showing  $\alpha$ -Al<sub>2</sub>O<sub>3</sub> being the dominant phase in the entire range of composition considered in the present work. The thermodynamic calculations predict that  $\beta$ -NiAl is in equilibrium with  $\alpha$ -Al<sub>2</sub>O<sub>3</sub> only at very reducing conditions (near 10<sup>-40</sup> atm) and it then becomes L1<sub>2</sub>-Ni<sub>3</sub>Al as oxygen partial pressure increases. Al in L1<sub>2</sub>-Ni<sub>3</sub>Al is further oxidized as oxygen chemical potential increases, and Ni<sub>3</sub>Al becomes fcc Ni. In the 10<sup>-16</sup> atm regime, the spinel phase (NiAl<sub>2</sub>O<sub>4</sub>) becomes more stable over  $\alpha$ -Al<sub>2</sub>O<sub>3</sub>, and then fcc Ni is further oxidized to halite (NiO) as the oxygen partial pressure increases. During the initial oxidation, NiO can co-exist either with NiAl<sub>2</sub>O<sub>4</sub> or with Al<sub>2</sub>O<sub>3</sub> at the surface where more oxygen is available (high PO<sub>2</sub>), depending on the composition of the substrate (Ni- or Al-rich). As the oxidation continues to evolve over time, the oxygen partial pressure decreases as a function of oxide scale thickness (from the gas/oxide interface toward the oxide/metal interface [22]), and as a result  $\alpha$ -Al<sub>2</sub>O<sub>3</sub> becomes a thermodynamically

**Fig. 8** Calculated stability diagram as a function of oxygen partial pressure (atm) in the Ni–Al–O system at 750 °C. The vertical line represents the exact  $\beta$ -NiAl stoichiometry



stable structure. The computational thermodynamic calculations predict that there is a correlation between real-time dynamic observations and thermodynamic modeling showing complementarity of both techniques. The thermodynamic predictions agree well with the experimental observations. Mainly, we observed both metastable and stable  $\text{Al}_2\text{O}_3$  with some incorporated Ni particles. At the gas/oxide interface, nanocrystals were observed and identified as NiO, which formed either in the initial stage of oxidation (high  $\text{PO}_2$  and local selective oxidation of Ni or local Al depletion in NiAl substrate) or, as shown in the previous section, due to the damage of oxide and the subsequent outward diffusion of Ni to the surface.

## Conclusions

In summary, the nanoscale oxidation behavior of  $\beta$ -NiAl was investigated using in situ closed-cell gas-reaction microscopy at elevated temperature (700–750 °C) in air at a pressure of 730 Torr under oxidizing gas conditions. Thermodynamic calculations suggest that the oxide scale formed under these conditions is composed of  $\text{Al}_2\text{O}_3$ , which agrees well with the real experimental data. Small faceted cubic crystals of NiO were formed at the initial stage of oxidation at high  $\text{PO}_2$  due to the outward self-diffusion of  $\text{Ni}^{2+}$  ions, followed by the formation of  $\text{Al}_2\text{O}_3$  scale beneath, as  $\text{PO}_2$  decreased with oxidation time at the oxide/metal interface, which agreed with thermodynamic modeling. After 92 s of oxidation at 750 °C, nucleation of voids at the substrate/ $\text{Al}_2\text{O}_3$  interface was observed, along with the subsequent outward diffusion of  $\text{Ni}^{2+}$  ions since Al was most likely exhausted at this stage to support reformation of the  $\text{Al}_2\text{O}_3$  scale. The microstructure of  $\text{Al}_2\text{O}_3$  was constructed of nano-size grains of both metastable (cubic) and stable (hexagonal)  $\text{Al}_2\text{O}_3$ . The oxide scale was thicker at higher temperature. Also, at higher temperature initial oxidation was faster, reaching a plateau in a shorter time than at lower temperature (700 °C). The in situ closed-cell gas reaction STEM characterization method presented in this study offers the potential to understand the fundamental high-temperature oxidation mechanisms and kinetics for a wide range of alloys.

**Acknowledgements** This research was supported by the U.S. Department of Energy, Office of Coal and Power R&D, Office of Fossil Energy (KAU, DS, LFA). Additional support was provided by the Center for Nanophase Materials Sciences, which is a U.S. Department of Energy Office of Science Scientific User Facility (RRU). The authors wish to thank K.L. More and B.A. Pint for providing comments on the manuscript.

## References

1. G. Frommeyer and R. Rablbauer, *Steel Research International* **79**, 2008 (507–513).
2. P. A. Pint, *Oxidation of Metals* **49**, 1998 (531–559).
3. J. Doychak, J. L. Smialek and T. E. Mitchell, *Metallurgical Transactions A* **20**, 1989 (499).
4. M. W. Brumm and H. J. Grabke, *Corrosion Science* **33**, 1992 (167–1690).
5. B. A. Pint, T. M. Treska and L. W. Hobbs, *Oxidation of Metals* **47**, 1997 (1–20).
6. B. A. Pint, J. R. Martin and L. W. Hobbs, *Oxidation of Metals* **39**, 1993 (167–195).

7. E. Schumann, J. C. Yang, M. J. Graham and M. Rühle, *Materials and Corrosion* **46**, 1995 (218–222).
8. E. Schumann, J. C. Yang, M. J. Graham and M. Rühle, *Materials and Corrosion* **47**, 1996 (631–632).
9. C.-M. Wang, A. Genc, H. Cheng, L. Pullan, D. R. Baer and S. M. Bruemmer, *Scientific Reports* **4**, 2014 (1–6).
10. C.-M. Wang, D. K. Schreiber, M. J. Olszta, D. R. Baer and S. M. Bruemmer, *Applied Materials & Interfaces* **7**, 2015 (17272–17277).
11. Q. Jeangros, T. W. Hansen, J. B. Wagner, R. E. Dunin-Borkowski, C. Hebert, J. Hessler-Wyser, et al., *Acta materialia* **67**, 2014 (362–372).
12. L. F. Allard, S. H. Overbury, W. C. Bigelow, M. B. Katz, D. P. Nackashi and J. Damiano, *Microscopy and Microanalysis* **18**, 2012 (656–666).
13. L. F. Allard, W. C. Bigelow, S. Zhang, X. Pan, Z. Wu, S. H. Overbury, et al., *Microscopy and Microanalysis* **20**, 2014 (1572–1573).
14. L. F. Allard, W. C. Bigelow, Z. Wu, S. H. Overbury, K. A. Unocic, M. Chi, et al., *Microscopy and Microanalysis* **21**, 2015 (97–98).
15. S. J. Pennycook, *Ultramicroscopy* **30**, 1989 (59–69).
16. G. C. Wood and B. Chattopadhyay, *Corrosion Science* **10**, 1970 (471–480).
17. J. Doychak and M. Rühle, *Oxidation of Metals* **31**, 1989 (431–452).
18. H. J. Grabke, *Intermetallics* **7**, 1999 (1153–1158).
19. M. W. Brumm, H. J. Grabke and B. Wagemann, *Corrosion Science* **36**, 1994 (37–53).
20. B. Pint, *Oxidation of Metals*. **48**, 1997 (303–328).
21. W. J. Quadakkers and M. J. Bennett, *Materials Science and Technology* **10**, 1994 (126–131).
22. B. Pint and K. L. More, *Journal of Materials Science* **44**, 2009 (1676–1686).